



# Moisture-gradient-enhanced ionic thermoelectrics

Received: 14 March 2025

Accepted: 29 October 2025

Published online: 12 December 2025

Check for updates

Chunyu Zhao<sup>1</sup>, Yidan Wu<sup>1</sup>, Dongxing Song<sup>②</sup>, Xing Zhang<sup>①</sup> & Weigang Ma<sup>①</sup>

Ionic thermoelectrics (i-TEs) demonstrate immense application potential in such fields as wearables and low-grade energy harvesting. Though adequate moisture absorption is required to facilitate ion dissociation in i-TEs, the impact of moisture gradient has been overlooked. Herein, we demonstrate a moisture-gradient-enhanced ionic thermoelectric generator (MGITG) driven by both moisture and temperature gradients. The MGITG exhibits an ionic thermopower of 34.02 mV K<sup>-1</sup>, a high open-circuit voltage of 644.19 mV, and an ultrahigh 1 h output energy density of 917.54 J m<sup>-2</sup>. We attribute the enhanced performance to fast and selective ion transport driven by coupled heat and moisture transfer. As a proof of concept, this material enabled the development of wearables capable of monitoring motion and respiration, as well as robotic systems equipped with synchronous environmental and tactile sensing. This work holds promise in the design of high-sensitivity, multifunctional, and high-energy-density i-TEs, facilitating their applications in robotic touch and wearables.

The thermoelectric conversion plays a crucial role in human society, as it not only enables the collection of widely available low-grade heat energy for power generation<sup>1,2</sup> but also serves as a basic principle of sensors<sup>3</sup>. Ionic thermoelectrics (i-TEs) have garnered significant attention due to their inherent flexibility and notable high thermopower (or Seebeck coefficient)<sup>4</sup>. Recent advancements in i-TEs have significantly enhanced their thermoelectric performance, encompassing the thermopower<sup>5,6</sup>, energy density<sup>7,8</sup>, among other parameters. However, limited by the capacitor mode, the energy density of i-TEs driven by the Soret effect is still much lower than that of i-TEs driven by the thermogalvanic effect<sup>9</sup>. Apart from its demonstrated potential in thermoelectric conversion<sup>10</sup>, i-TEs hold promise for applications in wearables<sup>11</sup> and robotic touch<sup>12</sup>. This is due to the ion transport in ion conductors affected by multiple factors such as temperature<sup>13,14</sup> and mechanical stress<sup>15,16</sup>. The output signals of i-TEs-based sensors indicate temperature and stress variations<sup>17</sup>. However, effective humidity detection methods for i-TEs remain unexplored. Humidity is a crucial component of biological perception, and sensing environmental humidity is one of the key challenges in intelligent sensing technology<sup>18</sup>. The development of humidity-sensitive, high-

energy-density i-TEs will significantly contribute to the advancement of multifunctional, highly sensitive, and self-powered micro-sensors<sup>19</sup>.

Most high-performance i-TEs rely on the high-humidity environment because moisture uptake facilitates ion solvation and causes the network to swell, resulting in faster ion diffusion<sup>20</sup>. The thermopower of the same material may vary several times in dry or humid environments<sup>21</sup>. Despite the existing research on i-TEs having emphasized the control of humidity<sup>22,23</sup>, harvesting energy from the moisture gradient<sup>18</sup> has been overlooked. Moisture-enabled electric generators (MEGs) harvest electricity through ubiquitous atmospheric moisture. A common type of MEGs is to utilize asymmetric ion movement under moisture<sup>24</sup>. However, existing MEGs rarely consider the thermodiffusion of ions. Considering similar ion transport characteristics, it is necessary to study the energy conversion in i-TEs from a broader perspective<sup>25</sup>. Compared to high-humidity environments, the design of the moisture gradient will endow i-TEs with more capabilities, helping them to break through the existing bottlenecks in thermoelectric performance.

From the view of the governing equation of i-TEs, the induced electric field is established due to the ion concentration gradient and

<sup>1</sup>Department of Engineering Mechanics, Key Laboratory for Thermal Science and Power Engineering of Ministry of Education, Tsinghua University, Beijing, China. <sup>2</sup>Key Laboratory of Process Heat Transfer and Energy Saving of Henan Province, School of Mechanics and Safety Engineering, Zhengzhou University, Zhengzhou, Henan, China. e-mail: [mawegang@tsinghua.edu.cn](mailto:mawegang@tsinghua.edu.cn)

temperature gradient within the ion conductor. The thermopower is closely related to parameters such as ion diffusion coefficients and Eastman entropy<sup>26</sup>. Classical governing equations do not take into account the influence of convective terms<sup>27</sup>. If the moisture diffusion is considered, it would generate new increments in the thermopower and induced potential<sup>28</sup>. Therefore, the synergistic utilization of temperature and moisture gradients is an ideal strategy for i-TEs. However, it remains a challenging problem to identify materials that are both excellent MEGs and ionic thermoelectric generators (i-TEGs), as well as to design devices that can couple the temperature gradient with the moisture gradient.

Herein, we proposed a moisture-gradient-enhanced ionic thermoelectric generator (MGITG), which utilizes the moisture gradient to enhance the performance of i-TEs (Fig. 1a). The MGITG can produce a high thermopower of  $34.02 \text{ mV K}^{-1}$ , a stable open-circuit voltage ( $V_{oc}$ ) of up to  $644.19 \text{ mV}$ , and a high energy density of  $917.54 \text{ J m}^{-2}$  at relative humidity (RH) of 90% and a temperature difference ( $\Delta T$ ) of 8 K. The  $V_{oc}$  and energy density are more than ten times that of most reported i-TEs<sup>29</sup>. Compared to high-humidity environments, the thermopower has increased by nearly 5 times, and the energy density has increased by an order of magnitude. We propose a “ $\pi$ ”-type series connection of pure p-type MGITG. The scalable integration of flexible and tailororable

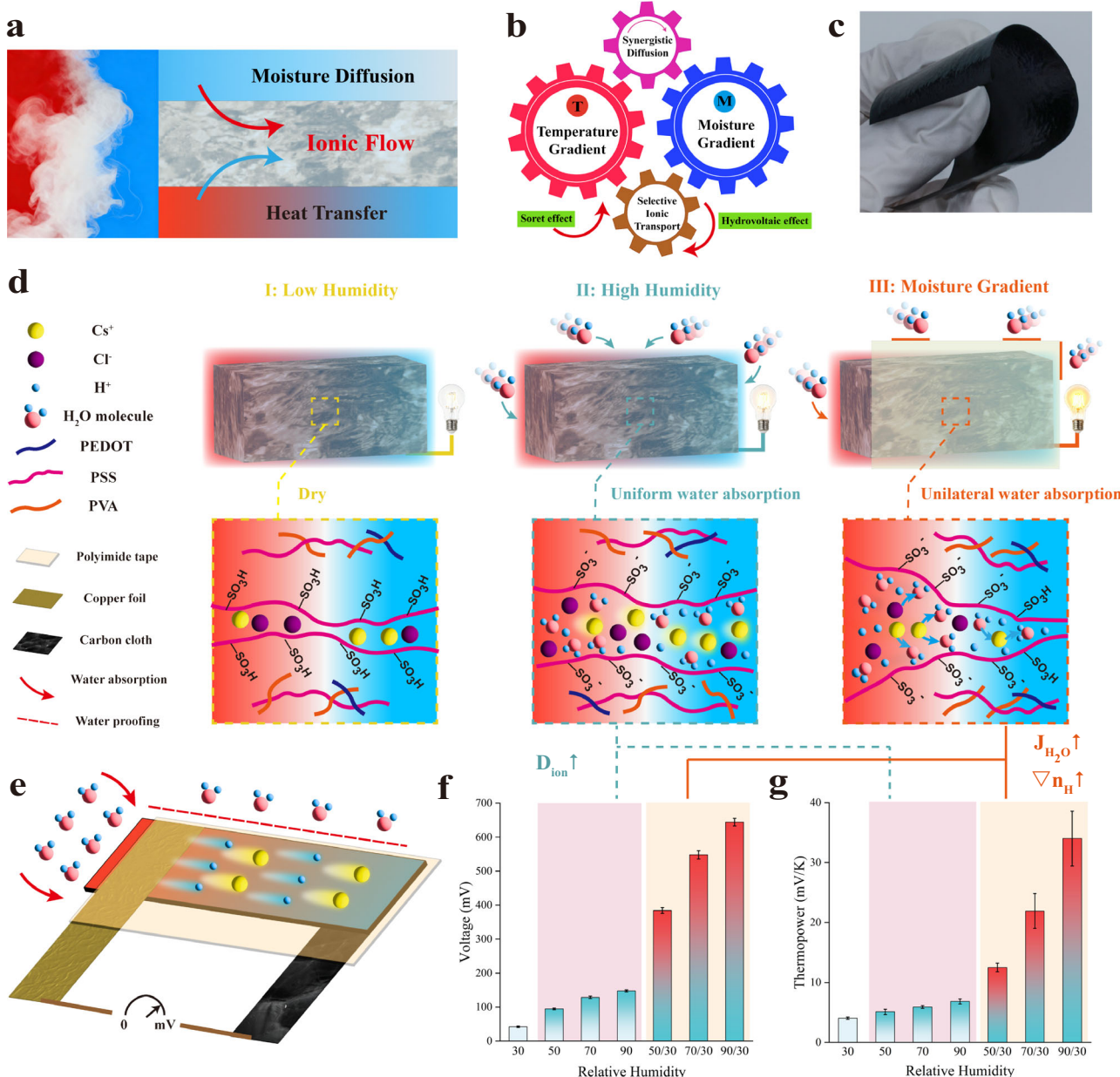


**Fig. 1 | Concept and thermoelectric performance of the MGITG.** **a** The coupling relationship among moisture diffusion, heat transfer, and ionic flow. Steam represents an abundant resource in both natural environments and industrial processes. The coupled transport of moisture and thermal energy, mediated by ion flux, enables highly efficient energy conversion. **b** The concept of moisture-gradient-enhanced i-TEs. The temperature gradient, moisture gradient, and selective ion transport act like three interlocking gears, with thermal-enhanced moisture diffusion creating synergistic effects that significantly improve the thermopower of i-TEs. **c** A photograph of the PEDOT:PSS/PVA/CsCl film. **d** Comparison of ion

transport in the MGITG under different conditions, including low humidity, high humidity, and moisture gradient. While dry conditions immobilize ions as pairs and uniform humidity enables cation migration without  $\text{H}^+$  gradient effects, moisture gradients drive cations (including  $\text{H}^+$ ) diffusion through microchannels. The MGITG uniquely couples thermal and moisture gradients for enhanced ion transport beyond conventional i-TEs. **e** A schematic diagram of the device structure. **f** The  $V_{oc}$  of the MGITG under 8 K and different RH conditions. **g** The thermopower of the MGITG under different RH conditions. Error bars in (g, h) were calculated using the standard deviation of the measured data.

MGITG can generate a voltage output above 5 V using exhaled breath (8-segment series). The MGITG possesses the ability to detect temperature, humidity, and stress, making it applicable for use in wearable devices and robots. The MGITG paves the way for high-sensitivity and high-energy-density i-TEs, and the utilization of the moisture gradient will elevate the performance of i-TEG to the next level.

## Results

### Design and characterization of the MGITG

Temperature and humidity are interconnected, and humid heat in the form of steam and vapor is ubiquitous. This implies that heat conduction is often accompanied by moisture diffusion (Fig. 1a). The existing governing equations for i-TEs simplistically account for the influence of RH as a change in the ionic diffusion coefficient, without considering the moisture diffusion, thereby neglecting the convective term in the governing equations. Considering the moisture diffusion simultaneously controlled by both temperature and moisture gradients, the flux of water molecules can be quantified by  $J_{H_2O} = -(D_{HH} \frac{\partial H}{\partial x} + D_{HT} \frac{\partial T}{\partial x})$  where  $D_{HH}$  and  $D_{HT}$  are the diffusion coefficients driven by moisture gradient and the humidity-temperature interaction, respectively.  $T$  and  $H$  are the temperature and humidity. Since cations and anions in i-TEs have different temperature dependence of the free energy (Eastman entropy  $\hat{S}_i$ ), we derived the expressions for thermopower and  $V_{oc}$  in the MGITG under the enhancement of the moisture gradient, as (see details in Supplementary A)

$$S'_{td} = \frac{\sum_i D_i \hat{S}_i n_i}{\sum_i D_i q_i e n_i} + \frac{k_B T}{F_{iw}} \frac{D_{HT}}{\sum_i D_i q_i e n_i} \quad (1)$$

where  $S'$ ,  $D$ ,  $n$ ,  $q$ ,  $e$  and  $k_B$  are the thermopower, diffusion coefficient, concentration of carriers, charge quantity, electron charge, and Boltzmann constant. The subscript “ $i$ ” indicates the  $i^{\text{th}}$  kind of ions, “td” indicates the thermodiffusion, and  $F_{iw}$  is the ion-water interaction factor, whose physical interpretation is the average hydration number per ion. The first term is for the thermopower of i-TEs, without considering the moisture gradient, i.e.,  $D_{HT} = 0$ . When considering the coupled diffusion of moisture and heat, an additional coupling term is introduced to the thermopower.

Similarly, the expression for the  $V_{oc}$  ( $U$ ) can be derived,

$$\frac{\partial U}{\partial x} = -\frac{\partial T}{\partial x} S'_{td} - \frac{\partial H}{\partial x} \left( \frac{k_B T}{F_{iw}} \frac{D_{HH}}{\sum_i D_i q_i e n_i} \right) \quad (2)$$

where the first term is temperature dependent and the second term (including  $D_{HH}$ ) is dependent on moisture gradient. The second term is independent of temperature, so it does not contribute to the thermopower. This model comprehensively considers the directional hydration-induced ion concentration difference and the Soret effect of i-TEs. We can observe that the temperature gradient, moisture gradient, and selective ion transport are like three interlocking gears (Fig. 1b). Since the temperature gradient can enhance moisture diffusion, the two have a synergistic effect, further enhancing the thermoelectric performance of i-TEs.

To simultaneously achieve remarkable thermoelectric and hydroelectric performance, poly(3,4-ethylenedioxythiophene):polystyrene sulfonate (PEDOT:PSS) and polyvinyl alcohol (PVA) are employed since they have good hydroscopicity and low thermal conductivity. Due to the high content of PSS in commercial PEDOT:PSS solutions, PEDOT:PSS is rich in hydrophilic functional groups (i.e.,  $-\text{SO}_3\text{H}$ )<sup>30</sup>. Upon exposure to a moist environment, the hydration of hydroscopic materials triggers the dissociation of sulfonic acid groups, releasing abundant  $\text{H}^+$  ions. The resulting concentration gradient drives the directional diffusion of these protons, further facilitated by continuous moisture flow, thereby establishing an electric potential between the electrodes and generating a stable voltage output<sup>31</sup>. The unique

structure of PEDOT:PSS (comprising PEDOT-rich and PSS-rich domains) forms nanochannels that facilitate efficient water uptake while establishing continuous percolation pathways. PVA forms interpenetrating hydrogen bonds with PSS chains, enhancing the mechanical properties and flexibility of PEDOT:PSS. This effectively reduces phase separation risk and enables conformal deformation to maintain persistent electrode contact under thermal cycling. Although PSS chains readily bind with certain cations ( $\text{Cu}^{2+}$ ,  $\text{Ni}^{2+}$ , or  $\text{In}^{3+}$ ), leading to anion-dominated diffusion in such cases<sup>32,33</sup>, the PEDOT:PSS/CsCl composite maintains p-type thermopower. The incorporation of PVA further facilitates  $\text{Cs}^+$  ion transport, due to the weak interactions between the oxygen atoms of the hydroxyl groups and  $\text{Cs}^+$  ions<sup>34</sup>. The polymer network of PEDOT:PSS-PVA is critical for facilitating the dissociation of  $\text{H}^+$  ions when absorbing moisture and also provides an appropriate pathway for cation diffusion. However, the change in entropy of  $\text{H}^+$  ions is low compared to other metal ions. The thermopower of i-TEs, with  $\text{H}^+$  ions as the main charge carriers, is usually not high<sup>35</sup>. Compared to  $\text{H}^+$  ions,  $\text{Cs}^+$  ions exhibit higher Eastman entropy, leading to greater thermal mobility of ions. They are also disruptors of local water structures (hydrogen bonds), thereby inhibiting anion transport<sup>36</sup>. Water microchannels significantly enhance  $\text{Cs}^+$  ion migration by facilitating CsCl dissociation under high humidity, thereby strengthening the ionic concentration gradient. As a result, the addition of cesium chloride (CsCl) introduced a large number of free  $\text{Cs}^+$  ions, thus improving the positive thermopower of the MGITG.

The MGITG is composed of PEDOT:PSS, PVA, and CsCl (abbreviated as PEDOT:PSS-PVA-CsCl). A free-standing film was formed after drying, as shown in Fig. 1c. Figure S1 illustrates the entire material preparation process. The electricity-generating film exhibits excellent mechanical properties, allowing it to be stretched and bent (Figs. S2 and S3). From the scanning electron microscope (SEM) images (Fig. S4), it can be observed that the surface of the film after humidity treatment exhibits more wrinkles or microscopic pores, indicating the formation of micro water channels. The functional groups of the MGITG were identified using Fourier Transform Infrared (FTIR) spectroscopy (Fig. S5). The spectral range from 1030 to 1200  $\text{cm}^{-1}$  includes the peak of C-O-C and S=O. The stretching vibrational band of S=O indicates the introduction of sulfonic acid groups<sup>37</sup>. Using differential scanning calorimetry (DSC) and the femtosecond laser time-domain thermoreflectance (TDTR) method, the heat capacity and thermal conductivity of the material were accurately measured, with detailed results shown in Fig. S6. The relatively low thermal conductivity ( $0.27 \text{ W m}^{-1} \text{ K}^{-1}$ ) is beneficial for maintaining a significant temperature difference.

To achieve stable moisture diffusion within the MGITG, most of the material is encapsulated with a thick polyimide (PI) tape, leaving only one end as the hydroscopic area. PI tapes exhibit excellent thermal stability (up to 260 °C) and superior moisture resistance. Before encapsulation, films are kept dry at 30% RH. In high-humidity environments, moisture will diffuse along the film. To clearly demonstrate the advantages of the MGITG, we compared the establishment process of the induced electric field under conditions of low humidity, high humidity, and moisture gradient (Fig. 1d). Here is a detailed comparison: (1) In low-humidity environments, ions are closely bound in the form of ion pairs. It is difficult for ions to migrate between tightly molecular chains, resulting in a very small  $V_{oc}$ . (2) In high-humidity environments, ions dissociate and exhibit cation-dominated migration. The material absorbs water and swells, causing the polymer chains to expand, which allows ions to have a higher diffusion coefficient, resulting in a higher  $V_{oc}$ . It is worth noting that although  $\text{H}^+$  ions also dissociate from PSS at this time, due to the absence of the  $\text{H}^+$  ion gradient, the moisture-induced voltage is not obvious. (3) In the case of the moisture gradient, on the side where moisture is taken up, ions dissociate and diffuse towards the drier side along with the moisture. Moisture diffusion leads to the formation of micro water channels

where the ion diffusion coefficient is exceptionally high. At the same time, the diffusion of  $H^+$  ions generates a very high  $V_{oc}$ . Further, the moisture diffusion is also regulated by the temperature gradient. The classic i-TEs only rely on the Soret effect to drive the differential motion of cations and anions under a temperature gradient. As for the MGITG, it simultaneously achieves selective ion transport driven by both temperature and moisture gradients.

To select suitable electrodes, we fully considered the capacitance (Fig. S7) and hydrophilicity/hydrophobicity (Fig. S8) of different electrodes. Using hydrophilic electrodes on the moisture-absorbing side leads to the rapid absorption of moisture, causing excessive swelling. Therefore, we use a hydrophobic-hydrophilic electrode combination. The moisture-absorbing side uses a hydrophobic electrode (copper foil) to prevent moisture accumulation, while the drying side uses a hydrophilic electrode (hydrophilic carbon cloth after plasma treatment). Although the sandwich structure provides a larger contact area, the  $V_{oc}$  test (Fig. S9) revealed that the moisture-induced voltage is unstable. Therefore, the copper electrode is placed above the moisture-absorbing side, and the carbon electrode is placed beneath the dry side (Fig. 1e). This design allows the utilization of both in-plane and out-of-plane moisture gradients, resulting in a more stable moisture-induced voltage. In high-humidity environments, the voltage stabilization time exceeds 8000 s, ensuring reliable thermoelectric performance measurements. Repeated testing demonstrated that the material maintained a voltage retention rate exceeding 75% after 4 h of continuous operation under 90% RH. The MGITG exhibits a shelf life exceeding 9 weeks with no observable voltage decay. The enhanced stability originates from three key design aspects: (1) the optimized electrode assembly, (2) robust encapsulation architecture, and (3) minimized exposed surface area ( $\sim 0.25\text{ cm}^2$ ).

The moisture gradient can significantly enhance the thermoelectric performance of i-TEs, including  $V_{oc}$ , thermopower, energy density, and so on. We conducted tests on the prepared MGITG under different humidity conditions. Moisture gradient can significantly increase  $V_{oc}$  because the diffusion of moisture significantly increases the rate of ion directional diffusion, with  $H^+$  ions being the most prominent. Figure 1f displays the  $V_{oc}$  of MGITG under different humidity conditions and  $\Delta T = 8\text{ K}$ . It can be observed that an increase in RH leads to a  $V_{oc}$  increase, from 41.78 mV at 30% RH to 147.54 mV at 90% RH. However, the moisture gradient has a more significant impact. A direct comparison between the  $V_{oc}$  of high humidity and moisture gradient shows that the voltage increased from 94.53 mV to 384.39 mV at 50% RH, which is a 307% increase. At 70% RH and 90% RH, the voltage enhancement due to the moisture gradient is 327% and 337%, respectively. The maximum  $V_{oc}$  of 644.19 mV was measured at 90% RH. It can be observed that even small temperature changes lead to significant voltage changes. Figure 1g displays the thermopower of the MGITG. It can be observed that the moisture-gradient strategy is also very effective in enhancing the thermopower. This is because the temperature difference also affects the diffusion of moisture, and the ion-selective diffusion is enhanced under the dual drive of temperature and moisture gradients. Taking the most significant enhancement (90% RH) as an example, the thermopower increased from 6.82 to 34.02 mV K $^{-1}$ , an increase of nearly 500%. This data demonstrates that the MGITG is not just a simple superposition of the MEG and i-TEG, but rather a synergistic effect of humidity and temperature gradients. The moisture gradient strategy can comprehensively enhance the thermoelectric performance of i-TEs and endow i-TEs with a rapid response capability to humidity.

### Electrical performance of an MGITG unit

A systematic study was conducted on the composition and proportions of the MGITG. The impact of different salt compositions on thermoelectric performance is shown in Fig. 2a, with a constant mass fraction of 33 wt% in the solid solution under  $\Delta T = 12\text{ K}$  and 90% RH. In the absence of salt addition, the  $V_{oc}$  of pure PEDOT:PSS and the

PEDOT:PSS-PVA mixture are 25.71 mV and 157.01 mV, respectively. After adding salt, the  $V_{oc}$  increases several times. This is due to an increase in mobile ions, as well as the enhanced hygroscopicity of the material. Among these ion sources, CsCl exhibits the highest  $V_{oc}$  of 613.11 mV. Other metal ions, such as  $Cu^{2+}$  and  $Li^+$ , easily form ion clusters with anions, thereby facilitating the diffusion of anions<sup>38</sup> and causing the thermopower to shift towards negative values. After confirming the use of CsCl, the optimal addition ratio was investigated to optimize the performance. The MGITG with CsCl mass fractions of 14%, 33%, 50%, and 60% in the solid were tested (Fig. 2b). At lower salt contents, increasing the salt addition significantly enhances the  $V_{oc}$ . This can be attributed to the increase in mobile ions, at which point the moisture absorption is excessive. However, after reaching 50%, further increasing the salt ratio results in a slight decrease in  $V_{oc}$ . This can be explained by the fact that the number of ions that moisture can dissociate reaches its limit, while the continuously enhanced ion-ion interactions hinder the transport of ions. A more detailed discussion on this will be presented in the next section. Subsequent measurements were conducted on MGITG with 50 wt% CsCl addition.

To further analyze the relationship between  $V_{oc}$  and moisture, the voltage curves under different humidity conditions were compared and analyzed (Fig. 2c). The first 2500 s of the test measured the voltage under 30% RH as the temperature difference was increased. The voltage rises slowly and tends to stabilize around 25 mV. Subsequently, the RH was rapidly increased in a constant temperature and humidity chamber, while the temperature difference was kept constant. The comparison found that the voltage curve corresponding to the moisture gradient would rapidly increase at the beginning of the test (approximately 1 min), which could be attributed to the rapid response of mobile ions dissociated and transported with moisture diffusion. Afterward, the effect of the temperature difference gradually became more apparent. More mobile ions diffuse towards the low-temperature end driven by the temperature difference. After 1000 s, the voltage tends to stabilize. The stabilized voltages under different moisture gradients are 384.39 mV (50% RH), 547.85 mV (70% RH), and 644.19 mV (90% RH), respectively. Figure S10 shows the ionic conductivity of the MGITG tested by electrochemical impedance spectroscopy (EIS) under different RH. It can be observed that the increase in RH significantly enhances the ionic conductivity. While the ionic conductivity of the dry side (30% RH) remains constant at  $4.79\text{ }\mu\text{S cm}^{-1}$ , the ionic conductivity on the moisture-absorbing side increases by an order of magnitude ( $36.23\text{ }\mu\text{S cm}^{-1}$  at 90% RH), indicating rapid unidirectional ion diffusion within the material. There was no voltage surge phenomenon in high-humidity environments. Their voltage eventually stabilizes at a level not exceeding 150 mV.

To further elucidate the critical role of thermal gradients in the MGITG, a comparative analysis of  $V_{oc}$  with and without temperature differences was essential. When the moisture gradient is maintained constant, the impact of temperature difference on the  $V_{oc}$  is analyzed (Fig. 2d). When the temperature difference increases from 0 to 12 K, the  $V_{oc}$  gradually rises from 432.97 to 786.51 mV. It can be seen that under a high moisture gradient, the sensitivity of  $V_{oc}$  to temperature also increases. At higher temperature differences, the contributions of temperature and moisture gradients to  $V_{oc}$  are comparable. In continuous tests, the stable voltage at different temperatures is measured, and the thermopower can be fitted (Fig. S11).

The energy density of i-TEG is generally limited by the charging mode of capacitors, leading to a rapid decay in power. However, moisture diffusion leads to continuous ion transport, which effectively increases the sustained discharge capability. Figure 2e shows the voltage curve of the MGITG over 3 charge-discharge cycles. The results show that the voltage returns to a relatively high level after each cycle, which is due to the continued migration of ions caused by the moisture diffusion. Although the temperature-induced voltage is difficult to maintain after multiple cycles, the moisture gradient still allows the

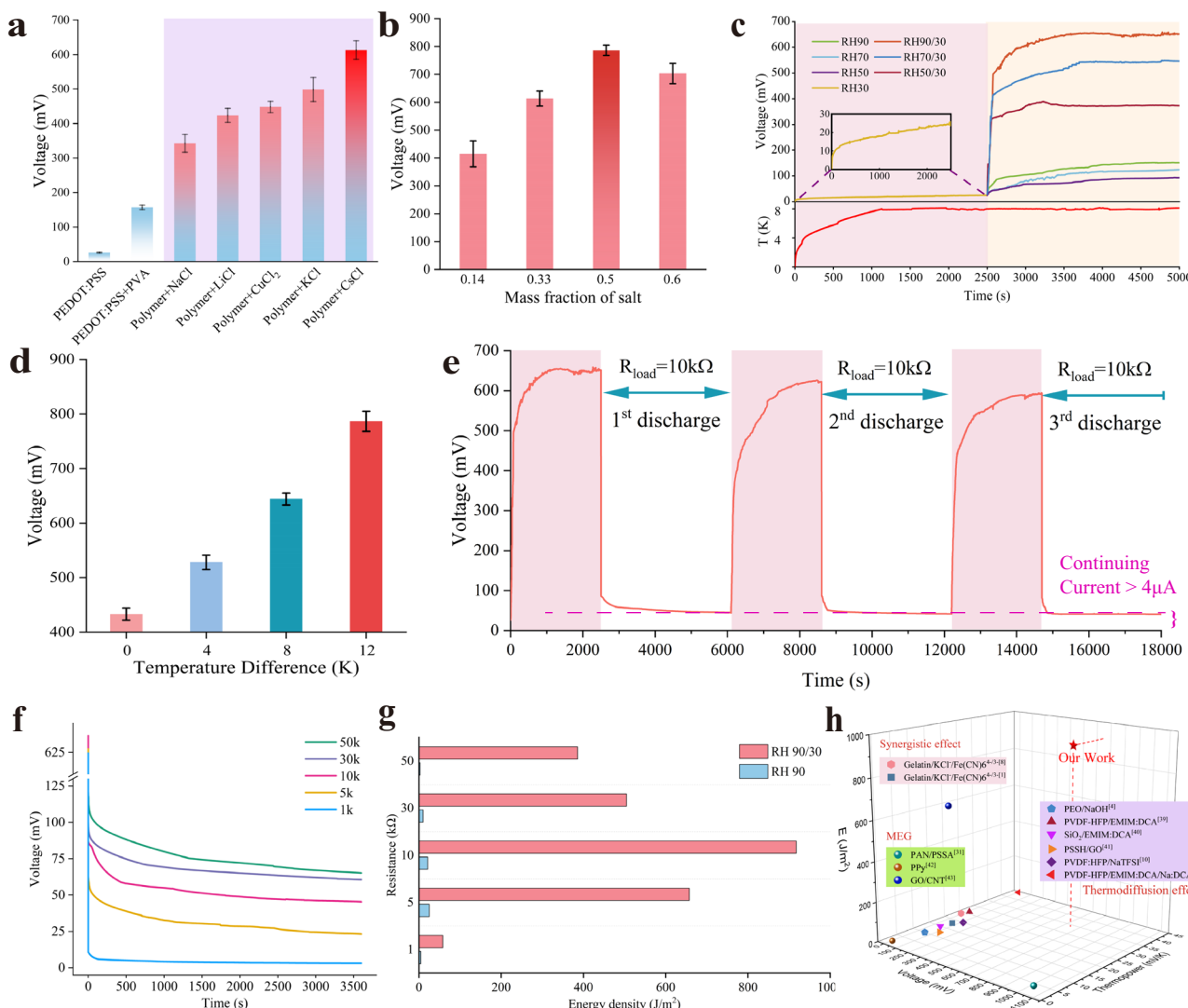


**Fig. 2 | Thermoelectric performance of an MGITG unit.** **a** The  $V_{oc}$  of different compositions under  $\Delta T=12$  K and 90% RH. **b** The  $V_{oc}$  of different mass fraction of CsCl. **c** Voltage-time curves under different humidity conditions. **d** The  $V_{oc}$  corresponding to variable temperature difference at 90% RH. The term “temperature difference” represents an absolute value. **e** Charge and discharge cycles while

maintaining a constant temperature difference 8 K and 90% RH. **f** Discharge curves of the MGITG under different external loads. **g** Comparison of energy density under different humidity and load conditions. **h** A performance comparison of the typical i-TEGs reported under  $\Delta T < 10$  K<sup>1,4,6,8,10,31,39–43</sup>. The error bars in (a, b, d) were calculated using the standard deviation of the measured data.

device to maintain good discharge power. A continuous current exceeding 4  $\mu$ A was maintained throughout the 3-h discharge process. Figure 2f shows the discharge curves of the MGITG under different loads. These curves exhibit two characteristics: (1) The initial voltage is very high, indicating a large discharge pulse at the initial stage; (2) After the rapid decay of discharging voltage, it remains at a relatively high level, enabling continuous discharge. By integrating the power over 1 h, energy densities were calculated under various loads, as shown in Fig. 2g. Tests revealed that the energy density peaks at 10 k $\Omega$ , reaching 917.54 J m<sup>-2</sup>. Compared to the high-humidity condition (the maximum energy density of 24.78 J m<sup>-2</sup> with external resistance of 5 k $\Omega$ ), there is a nearly 40-fold increase. From the discharge curve, it can be seen that the presence of a moisture gradient results in a higher  $V_{oc}$ , with high discharge power during the initial stage of discharging. In the middle and later stages of discharge, due to the maintained moisture gradient, cations continue to migrate to the cold end, causing the discharge current to remain higher than in the absence of a moisture gradient. The discharge power with a moisture gradient is an order of magnitude higher than without it, significantly enhancing the energy density and power density of the device.

Through optimization of the component ratios and device structure, the MGITG exhibited the optimal thermopower of 34.02 mV K<sup>-1</sup>,  $V_{oc}$  of 644.19 mV, and the energy density of 917.54 m<sup>-2</sup> under  $\Delta T=8$  K and 90% RH. As illustrated in Fig. 2h and Table S1, the MGITG significantly outperforms most i-TEG reported previously, especially in the  $V_{oc}$  and energy density. Although many studies have increased the thermopower to above 30 mV K<sup>-1</sup> through various methods, the  $V_{oc}$  is often below 100 mV. The ultra-high  $V_{oc}$  makes MGITG exhibit greater potential in energy harvesting and sensing. The energy density of the MGITG is higher than that of many reported high-performance i-TEGs with redox couples. It demonstrates that the i-TEG without redox couples could also be capable of simultaneously achieving high energy density and thermopower.

#### Mechanism verification of the MGITG

For the direct check of Cs<sup>+</sup> ion transport, two PEDOT:PSS/PVA/CsCl films were quickly dried under vacuum by a lyophilization treatment when they worked at  $\Delta T=8$  K and 90% RH. One is the MGITG, and the other film is the i-TEG only driven by  $\Delta T$ . Five points in each film were chosen for energy dispersive spectrometer (EDS) mapping in the

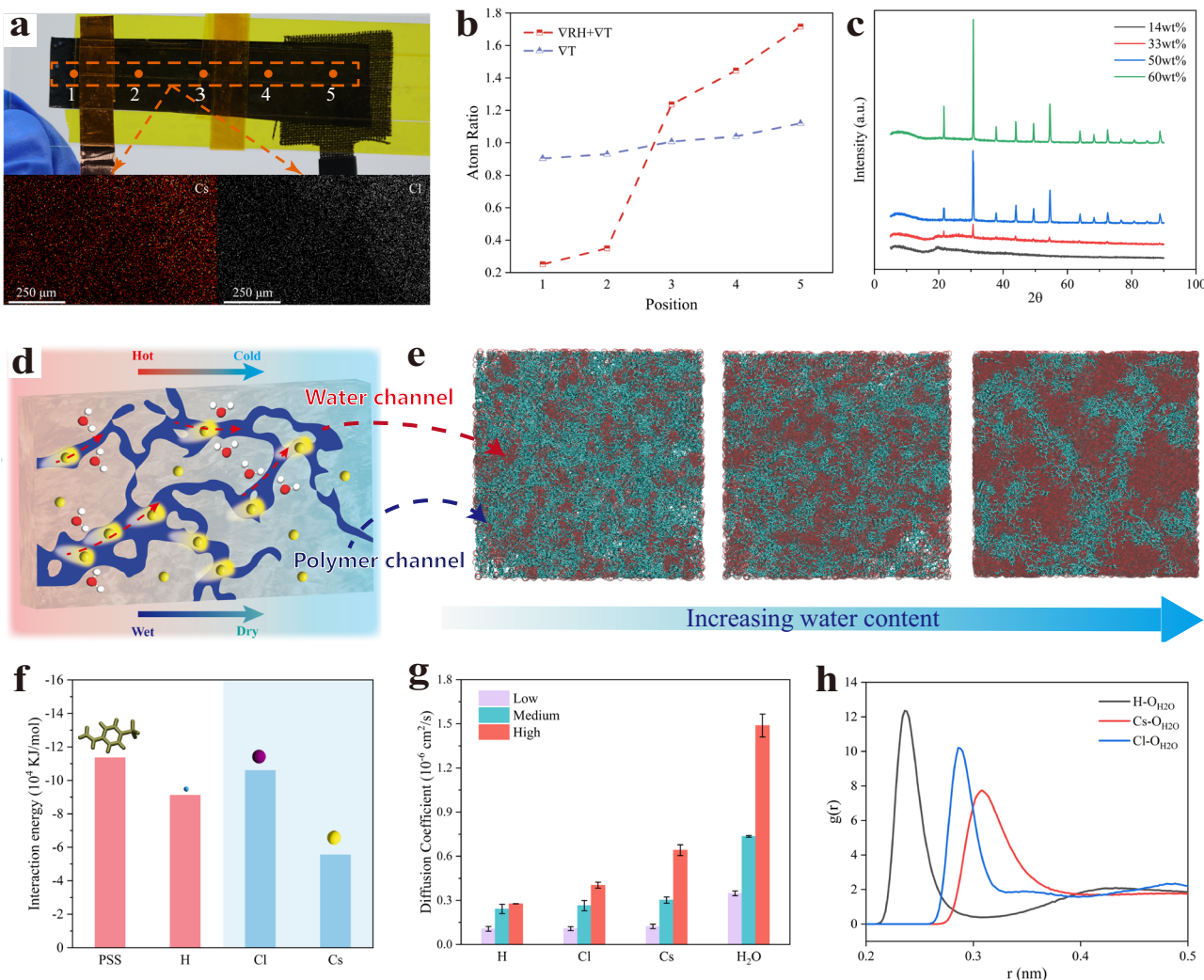


**Fig. 3 | Mechanism verification of the MGITG.** **a** A photograph of the MGITG film with electrodes, EDS maps of  $\text{Cs}^+$  and  $\text{Cl}^-$  ions between points 2 and 3. **b** Ratio of local Cs atomic% to the average Cs atomic% at the five selected points measured from EDS mapping. **c** XRD results at different salt mass fractions. **d** Conceptual diagram of moisture diffusion path inside the MGITG. **e** MD Simulation model of

the MGITG with different water contents. **f** Interaction energy with water of different molecules. **g** Diffusion coefficients of different components under different water contents, where the error bars were calculated using the standard deviation of the calculated data. **h** Radial distribution functions of different ions relative to oxygen atoms in water.

direction from hot to cold and from wet to dry. The EDS maps of  $\text{Cs}^+$  and  $\text{Cl}^-$  ions between points 2 and 3 in the MGITG are shown in Fig. 3a, and the comparison of the atomic ratio of  $\text{Cs}^+$  ions at different points between i-TEG and MGITG is displayed in Fig. 3b. In the MGITG, the atomic ratio of  $\text{Cs}^+$  ions at the cold side is more than five times that at the hot side, indicating a clear transport of  $\text{Cs}^+$  ions and gathering at the cold side. In the i-TEG, the gradient of the atomic ratio of  $\text{Cs}^+$  ions is significantly decreased. The comparison points out that the ion concentration difference caused by coupled heat and moisture transfer is much larger than the thermal-induced ion concentration difference. The EDS results directly support the mechanism of moisture-gradient-enhanced i-TEs.

Characterization techniques can explain the optimal ratio of  $\text{CsCl}$  addition and rule out potential chemical reactions at the electrodes. From the X-ray diffraction (XRD) results (Fig. 3c), distinct XRD peaks corresponding to  $\text{CsCl}$  crystallization become prominently visible when the  $\text{CsCl}$  concentration exceeds 50 wt% in the composite. At 60 wt%  $\text{CsCl}$  loading, the XRD peak intensities exhibit further enhancement, with the dominant peak at  $2\theta = 30^\circ$  showing a 74% increase in intensity. This pronounced amplification indicates substantial growth of crystalline  $\text{CsCl}$  domains. The X-ray photoelectron spectroscopy (XPS) results

(Fig. S12) show the 3d peak of  $\text{Cs}$  atoms, and it can be observed that as the salt content increases, the two peaks corresponding to 3d are noticeably elevated, while the peak positions shift towards the lower binding energy direction. This indicates that the  $\text{Cs}$  added more than 50 wt% mainly exist in the form of ion pairs. Based on the data in Fig. 2b, it indicates that for the MGITG, an appropriate amount of ion crystallization is beneficial for selective ion transport. Adding 50 wt%  $\text{CsCl}$  is optimal, as adding more salt leads to excessive ion-ion interactions, which inhibit ion diffusion. We also performed XPS characterization on the Cu  $2p$  peak positions (shown in Fig. S13), indicating that no new reaction products were formed. These characterization techniques provide direct evidence for understanding the interactions between ions and the polymer, verifying whether the developed materials contain an optimal ion source incorporation.

Molecular dynamics (MD) simulations are performed to understand the atomic interactions in the PEDOT:PSS/PVA/ $\text{CsCl}$  system (see details in “Methods”). Figure 3d, e explains why the moisture gradient is so important in ion diffusion. In the simulation, it can be observed that multiple water channels are formed within the PEDOT:PSS (the red areas in Fig. 3e). With the increase in water content, the proportion of water

channels significantly increases. On one hand, ions have a very high diffusion coefficient within these channels. On the other hand, the high diffusion rate of water also carries a large number of ions. The cations exhibiting greater Eastman entropy were found to substantially boost the positive thermopower of the system. By calculating the diffusion barrier (Fig. S14), it can be found that the introduction of PVA significantly increases the diffusion barrier of  $H^+$ , resulting in an increase in the Eastman entropy of cations<sup>44</sup>. Furthermore, the Eastman entropy of cations in the PEDOT:PSS/PVA/X (X = NaCl, CuCl<sub>2</sub>, CsCl) system was computationally determined while maintaining the same proportional composition of all components. The calculated entropies for Na, Cu, and Cs were  $775.47\text{ J K}^{-1}\text{ mol}^{-1}$ ,  $783.57\text{ J K}^{-1}\text{ mol}^{-1}$ , and  $801.06\text{ J K}^{-1}\text{ mol}^{-1}$ , respectively, showing a clear ascending trend. These results align well with experimental measurements (shown in Fig. 2a). From the results of the interaction energy calculations (Fig. 3f), the trend of water dissociation from PSSH is stronger, hence the concentration gradient of hydrogen ions is established first in the system. This can also explain why there is a voltage jump at the initial moment during voltage testing. From the statistical results of the diffusion coefficients in Fig. 3g, the ions are arranged in descending order of diffusion coefficients as Cs<sup>+</sup>, Cl<sup>-</sup>, and H<sup>+</sup>, and the diffusion coefficient of water is the highest. This indicates that the transport of water molecules is dominant and is capable of carrying other ions along with them. Due to the different binding strengths between ions and water, polymers, the ion diffusion coefficients from high to low are Cs<sup>+</sup> > Cl<sup>-</sup> > H<sup>+</sup>. From the radial distribution function (RDF) results (Fig. 3h), H is most tightly bound to water, followed by Cl<sup>-</sup> and Cs<sup>+</sup>. Despite the stronger interaction between Cl<sup>-</sup> and water, the solvation process of Cl<sup>-</sup> also produces a large amount of free Cs<sup>+</sup>. MD simulations theoretically demonstrate the fast and selective ion transport caused by moisture diffusion, which can be mutually confirmed with experimental results.

### Scalable integration

To achieve larger-scale applications, the prepared films need to be connected in series and/or parallel. Figure S15 shows the  $V_{oc}$  tested under the same conditions for 2, 4, 6, and 8 units connected in series. It can be observed that as the number of series connections increases, the  $V_{oc}$  increases linearly. For thermoelectric materials, the most efficient connection method is the  $\pi$ -type series connection, which requires alternating *p*-type and *n*-type materials. In this way, hot and cold ends can be distributed on both sides, helping to maintain a stable temperature difference and maximize energy conversion efficiency. However, high-thermopower *n*-type i-TEs are relatively rare. This is due to the lack of high-entropy anions like metal cations<sup>45</sup>. This paper innovatively proposes a  $\pi$ -type series connection for pure *p*-type materials. The PI tape with properties of thermal insulation and moisture barrier is chosen to encapsulate the series-connected MGITG units. Every unit has one side exposed, with the upper and lower sides arranged alternately, as shown in Fig. 4a. When this device is placed in a high-temperature and high-humidity environment, the hot and humid vapor can alternately enter from the upper and lower ends of the series-connected units. This innovative series connection method fully leverages the advantages of the MGITG. Efficiently connecting high-performance materials in series can lead to a significant enhancement in the performance of ionic thermoelectric devices. Furthermore, it is convenient to scale up the series-connected units into large-scale 3D integration, as shown in Fig. 4b. This provides a strategic approach for high-sensitivity, self-powered wearable devices.

The MGITG demonstrates significant applicability in wearable devices, particularly in respiration monitoring, temperature sensing, and action recognition. Figure 4c shows the voltage response curves corresponding to exhalation and motion. In response to exhaled breath, an MGITG unit can generate a voltage of approximately 250 mV and 500 mV for shallow and deep breaths, respectively. This is due to differences in the humidity of exhaled breath. Since the moisture

content in a single exhalation is low and the sensing area is relatively small, the voltage quickly returns to its initial level within about 10 s. After connecting 8 units, it can be seen that after one deep breath, the device's  $V_{oc}$  can reach 5 V before falling back. This allows simultaneous recording of breathing frequency and depth, thereby inferring information such as exercise status. The very high  $V_{oc}$  makes the device more sensitive to environmental changes, significantly improving sensitivity and presenting great application prospects. In addition to responding to moisture and temperature, the MGITG also exhibits excellent response characteristics to force. The lower part of Fig. 4c shows the test results of the voltage changes in response to finger bending after fixing the unit on the finger.

Beyond its application in wearable devices, the MGITG also demonstrates significant potential for use in robotic tactile sensing. Figure 4d shows the material attached to the fingers of a robotic hand, with a sealed MGITG unit and a normal MGITG unit applied to the two sides of the finger. They will have different voltage response curves. For the sealed MGITG, it will only respond to temperature, as the humidity-sensitive area is also encapsulated. The normal MGITG, responds to both temperature and humidity simultaneously, allowing the approximate range of environmental temperature and humidity to be determined from the voltage (as indicated by the red dashed line in the Fig. 4d). By combining this with the temperature range (see details in Table S2) measured by the sealed MGITG, accurate sensing of both temperature and humidity can be achieved. As a result, an ion skin for robots composed of many MGITG units can sense humidity and temperature, which holds promise for applications in smart inspection. In terms of response time, the first voltage plateau induced by humidity variation emerges at approximately 9 s. Although the voltage stabilization process triggered by temperature changes requires a longer duration, the maximum voltage variation within 30 s still effectively reflects the temperature information.

Figure 4e further demonstrates the application of MGITG as a flexible temperature and humidity sensor in detecting the temperature and humidity of grasped objects. The sensor was placed on the palm of a robotic hand, which was used to grasp towels in different conditions. Before testing, the same towels were stored for 1 h in a constant temperature and humidity chamber under the following conditions: 30% RH and 30 °C, 30% RH and 50 °C, 90% RH and 30 °C, and 90% RH and 50 °C. Based on the voltage response curves (response speed and magnitude), it can determine whether the towel is hot or cold, dry or wet. These two application cases fully demonstrate the significant role of MGITG in intelligent sensing. It enables robotic hands to sense environmental temperature and humidity, and perceive the state of the objects they grasp, much like human hands.

### Discussion

We have established a more universal governing equation for i-TEs, incorporating a convective term induced by moisture diffusion. The derived expressions for  $V_{oc}$  and thermopower demonstrate that the synergistic diffusion of moisture and heat leads to significant performance improvements. We developed an MGITG to validate the feasibility of enhancing thermoelectric performance through moisture gradients. The strategy effectively increases the thermopower to  $34.02\text{ mV K}^{-1}$ ,  $V_{oc}$  to  $644.19\text{ mV}$ , and energy density (1 h) to  $917.54\text{ J m}^{-2}$  under  $\Delta T = 8\text{ K}$  and 90% RH. These excellent results are much higher than most i-TEGs reported previously, driven by a small temperature difference ( $\Delta T < 8\text{ K}$ ). For large-scale applications, we propose a practical  $\pi$ -type series connection composed of pure *p*-type i-TEs. The MGITG exhibits excellent temperature and humidity sensing capabilities, which hold promise for applications in wearables and robotic tactile sensing. However, future development of the MGITG is still needed, particularly in using advanced technologies for the mass production and assembly of i-TE devices, with a focus on multiphysics coupling processes and targeted structural design. Nevertheless, our

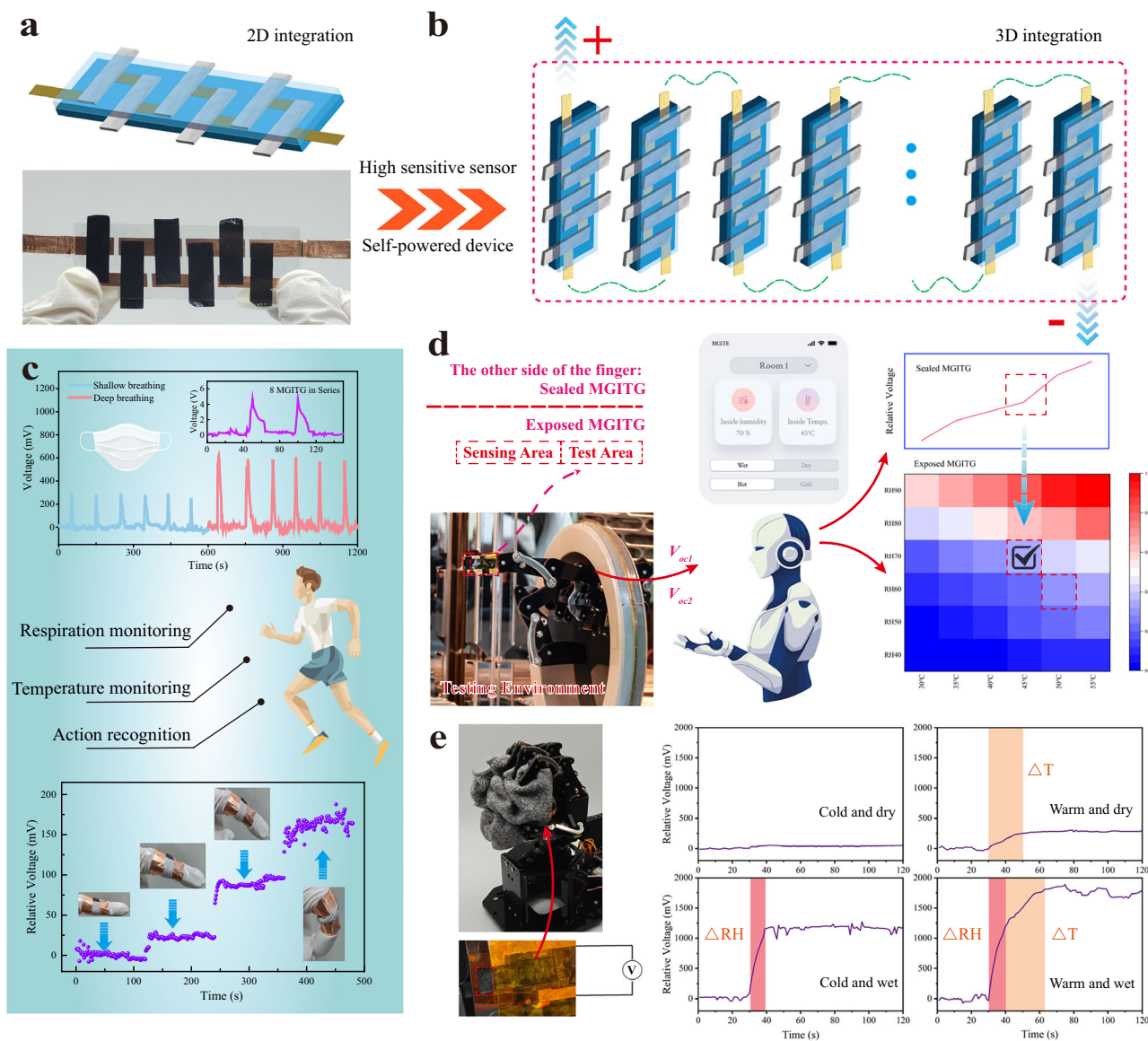


**Fig. 4 | The integration and application of the MGITG.** **a** Schematic diagram of π-type series connection for pure p-type MGITG and the corresponding device picture. **b** Schematic diagram of 3D integration of the MGITG. **c** Application examples on wearable devices include respiration monitoring and action recognition. **d** The MGITG fixed on the robotic arm enables it to sense the temperature and humidity

of the environment. By comparing the voltage response curves of two MGITGs (one is completely encapsulated and not hygroscopic), the specific values of temperature and humidity can be quickly determined. **e** The application in robotic tactile sensing involves detecting the temperature and humidity state of grasped objects. Towels under different temperature and humidity were used for grasping tests.

work introduces a promising paradigm for energy conversion and application of i-TEs, with a focus on the moisture diffusion within i-TEs under the temperature gradient. Our study demonstrates that advancing i-TE requires a holistic research perspective that systematically unifies moisture transport, ion migration, and thermal conduction mechanisms. This will help drive the development of i-TEs towards higher voltage and energy density, marking a significant step forward in the practical application of i-TEs.

## Methods

### Material

PEDOT:PSS (1.5 wt% in water, PEDOT:PSS = 1:6), PVA (Alcoholysis degree: 87.0–89.0 mol%, viscosity: 80.0–110.0 mPa s), CsCl ( $\geq 99.99\%$  metals basis), NaCl ( $\geq 99.99\%$  metals basis), CuCl<sub>2</sub> ( $\geq 99.99\%$  metals basis) and LiCl ( $\geq 99.99\%$  metals basis) were purchased from Aladdin Industrial Corporation. PI tapes (the thickness is 0.055 mm) and copper foil tapes (the thickness is 0.036 mm) used for encapsulation were purchased from 3 M Company. Hydrophilic carbon cloth (WOS1009,

the thickness is 0.36 mm) used for the electrode was purchased from Beijing Zhongke Yannuo New Material Technology Co., Ltd. All chemical reagents were employed without further purification.

### Preparation of PEDOT:PSS-PVA-CsCl film

To prepare the film, a 5 wt% aqueous solution of PVA and a 1.5 wt% aqueous solution of PEDOT:PSS were pre-mixed at a polymer mass ratio of 1:1. CsCl was then added to the polymer solution with different mass fractions and stirred at room temperature for 6 h. To increase the thickness of the film, 40% of the water in the solution was evaporated when stirring on a hot plate at 600 rpm and 40 °C. The prepared solution was poured into a polytetrafluoroethylene mold and heated at 40 °C for approximately 12 h. After film formation, the prepared film was scraped off the base. To avoid curling during the cooling process, the film was clamped with two glass slides and pressed with a weight for 6 h. The width and thickness of the film were precisely controlled at 1 cm and 110  $\mu$ m, respectively. The prepared thin films were encapsulated in a glove box for future use.

## Preparation of MGITG

A combination of hydrophobic and hydrophilic electrodes was adopted. The carbon cloth was plasma-treated to enhance its hydrophilicity. Copper foils (hydrophobic electrodes) and hydrophilic carbon cloth (hydrophilic electrodes) were placed at both ends and on the upper and lower sides of the film. The copper electrode was pre-attached to the glass substrate with an interelectrode spacing of approximately 3.5 cm. Except for the portion of the film exposed on the moisture-entry side, the rest of the film was encapsulated with PI tapes.

## Thermoelectric performance test

The entire experimental setup was placed inside a temperature- and humidity-controlled chamber (Duohe, DHTH-100-70-P-ES). During testing, the chamber temperature was consistently maintained at 30 °C, while RH was adjusted according to testing requirements. When testing the effect of the moisture gradient, the MGITG was left to stabilize in the chamber at 30% RH for 6 h. After the voltage stabilized, the relative humidity was set to the target value and reached within approximately 2–4 min. A high-precision hygrometer is used to monitor the surface humidity of the material, ensuring that humidity fluctuations remain within  $\pm 1\%$  upon reaching the set humidity level. For a stable temperature difference, one Peltier heater and one Peltier cooler were located under the tested materials, powered by two Advantest R6243 source meters, providing a temperature difference along the length direction of the film. The thermal voltages produced by the MGITG were recorded with a nano-voltage meter (Keithley 2002). Two T-type thermocouples were applied to record temperature variation between the hot and cold sides of MGITG controlled by NI 9213 coupled with NI 9162 modes. To ensure optimal contact between the material and electrodes, a constant pressure of 200 g was continuously applied at both electrode locations throughout the testing process. The whole test system was first calibrated well with the reported *i*-TE materials in the previous work.

## Characterization

A scanning electron microscope (SEM, ZEISS-Merlin) was used to characterize the morphology of the materials. The XPS measurement was conducted using Thermo Fisher ESCALB Xi+. The XRD measurement was conducted using Rigaku-MiniFlex600. The FTIR measurement was conducted using Netzsch-X70.

## The ionic electrical conductivity measurement

The ionic conductivity of the *i*-TE materials was determined by the EIS measurement in a frequency range from 100 kHz to 0.1 Hz using two stainless steel block electrodes with a diameter of 1 cm. The measurements were conducted using an electrochemical workstation (Autolab PGSTAT302N, Metrohm). The ion conductivity was calculated according to  $\sigma_{\text{ion}} = I/R_{\text{total}}A$ , where  $I$  and  $A$  are the thickness and contact area of the materials, respectively.  $R_{\text{total}}$  is equal to  $R_b + R_i$ . They are obtained based on the first semicircle of the impedance spectrum through equivalent circuit fitting.

## Thermal conductivity measurement

The TDTR method was used to measure the thermal conductivity  $k_{\text{MGITG}}$ . First, we performed conventional TDTR measurements on an Al-coated  $\text{SiO}_2$  substrate to determine the thermal conductivity of  $\text{SiO}_2$  and the interfacial thermal conductance. Subsequently, bidirectional TDTR measurements were conducted on samples with the spin-coated MGITG. The thermal conductivity of the sample was extracted through fitting the experimental data to our thermal model<sup>46</sup>. To ensure measurement reliability and minimize experimental uncertainties, measurements were performed at three randomly selected locations across each sample, with three repeated measurements conducted at each location. The specific heat capacity was obtained using DSC (TA instruments-DSC250).

## MD simulation

Classical all-atom MD simulations were conducted using the Gromacs software (version 2022.7.4)<sup>47</sup>. The initial configuration for each system was established by Packmol<sup>48</sup>. Structural optimization was carried out using the Generalized Amber Force Field<sup>49</sup>. Temperature and pressure were maintained using the V-rescale thermostat<sup>50</sup> and the Parrinello-Rahman barostat<sup>51</sup>, respectively. Long-range electrostatic interactions were computed using the particle-mesh Ewald method<sup>52</sup>. Simulations employed a time step of 1 fs, and visualizations were created with the VMD software<sup>53</sup>. The code for entropy calculation is referenced in our previous work<sup>26</sup>.

## Data availability

The source data used in this study are available in the Figshare database (<https://doi.org/10.6084/m9.figshare.29613458>)<sup>54</sup>. Additional data are available from the corresponding author upon request.

## References

1. Han, C. et al. Giant thermopower of ionic gelatin near room temperature. *Science* **368**, 1091–1098 (2020).
2. Wang, Y. et al. In situ photocatalytically enhanced thermogalvanic cells for electricity and hydrogen production. *Science* **381**, 291–296 (2023).
3. Dobashi, Y. et al. Piezionic mechanoreceptors: force-induced current generation in hydrogels. *Science* **376**, 502–507 (2022).
4. Zhao, D. et al. Ionic thermoelectric supercapacitors. *Energy Environ. Sci.* **9**, 1450–1457 (2016).
5. Zhou, Y. et al. Ion exchange induced efficient N-type thermoelectrics in solid-state. *Adv. Funct. Mater.* **33**, 2214563 (2023).
6. Liu, Z. et al. Giant thermoelectric properties of ionogels with cationic doping. *Adv. Energy Mater.* **12**, 2200858 (2022).
7. Zhang, W. et al. Gigantic and continuous output power in ionic thermo-electrochemical cells by using electrodes with redox couples. *Adv. Sci.* **10**, 2303407 (2023).
8. Li, Y. et al. 3D hierarchical electrodes boosting ultrahigh power output for gelatin-KCl-FeCN4-/3- ionic thermoelectric cells. *Adv. Energy Mater.* **12**, 2103666 (2022).
9. Lei, Z., Gao, W. & Wu, P. Double-network thermocells with extraordinary toughness and boosted power density for continuous heat harvesting. *Joule* **5**, 2211–2222 (2021).
10. Chi, C. et al. Reversible bipolar thermopower of ionic thermoelectric polymer composite for cyclic energy generation. *Nat. Commun.* **14**, 306 (2023).
11. Xia, M. et al. Self-powered multifunction ionic skins based on gradient polyelectrolyte hydrogels. *ACS Nano* **16**, 4714–4725 (2022).
12. Sun, W. et al. Heat source recognition sensor mimicking the thermosensation function of human skin. *Innovation* **5**, 100673 (2024).
13. Qian, X., Ma, Z., Huang, Q., Jiang, H. & Yang, R. Thermodynamics of ionic thermoelectrics for low-grade heat harvesting. *ACS Energy Lett.* **9**, 679–706 (2024).
14. Zhao, D. et al. Polymer gels with tunable ionic Seebeck coefficient for ultra-sensitive printed thermopiles. *Nat. Commun.* **10**, 1093 (2019).
15. Jia, L. et al. Giant iontronic flexoelectricity in soft hydrogels induced by tunable biomimetic ion polarization. *Adv. Mater.* **36**, 2403830 (2024).
16. Guan, X. et al. Spider webs-inspired aluminum coordination hydrogel piezionic sensors for tactile nerve systems. *Adv. Funct. Mater.* **35**, 2414016 (2024).
17. Zhao, W., Lei, Z. & Wu, P. Mechanically adaptative and environmentally stable ionogels for energy harvest. *Adv. Sci.* **10**, e2300253 (2023).
18. Xu, J. et al. Sustainable moisture energy. *Nat. Rev. Mater.* **9**, 722–737 (2024).

19. Zhang, H. et al. High-performance, highly stretchable, flexible moist-electric generators via molecular engineering of hydrogels. *Adv. Mater.* **35**, 2300398 (2023).

20. Liu, S. et al. High p- and n-type thermopowers in stretchable self-healing ionogels. *Nano Energy* **100**, 107542 (2022).

21. Zhao, Y. et al. Quasi-solid conductive gels with high thermoelectric properties and high mechanical stretchability consisting of a low cost and green deep eutectic solvent. *J. Mater. Chem. A* **10**, 4222–4229 (2022).

22. Zhao, D. et al. The role of absorbed water in ionic liquid cellulosic electrolytes for ionic thermoelectrics. *J. Mater. Chem. C* **10**, 2732–2741 (2022).

23. Song, D. et al. Conveyor mode enabling continuous ionic thermoelectric conversion. *Joule* **8**, 3217–3232 (2024).

24. Xu, T., Ding, X., Cheng, H., Han, G. & Qu, L. Moisture-enabled electricity from hygroscopic materials: a new type of clean energy. *Adv. Mater.* **36**, 2209661 (2024).

25. Bai, J. et al. Vapor and heat dual-drive sustainable power for portable electronics in ambient environments. *Energy Environ. Sci.* **15**, 386–396 (2022).

26. Chi, C. et al. Selectively tuning ionic thermopower in all-solid-state flexible polymer composites for thermal sensing. *Nat. Commun.* **13**, 221 (2022).

27. Qian, X., Liu, T. & Yang, R. Confinement effect on thermopower of electrolytes. *Mater. Today Phys.* **23**, 100627 (2022).

28. Yan, H., Liu, Z. & Qi, R. A review of humidity gradient-based power generator: Devices, materials and mechanisms. *Nano Energy* **101**, 107591 (2022).

29. Sun, S., Li, M., Shi, X. L. & Chen, Z. G. Advances in ionic thermoelectrics: from materials to devices. *Adv. Energy Mater.* **13**, 2203692 (2023).

30. Lu, B. et al. Pure PEDOT:PSS hydrogels. *Nat. Commun.* **10**, 1043 (2019).

31. Sun, Z. et al. Nanofiber fabric based ion-gradient-enhanced moist-electric generator with a sustained voltage output of 1.1 volts. *Mater. Horiz.* **8**, 233–239 (2021).

32. Kim, B., Hwang, J. U. & Kim, E. Chloride transport in conductive polymer films for an n-type thermoelectric platform. *Energy Environ. Sci.* **13**, 859–867 (2020).

33. Shu, Y. et al. Cation effect of inorganic salts on ionic Seebeck coefficient. *Appl. Phys. Lett.* **118**, 103902 (2021).

34. Jing, Z. et al. Hydration of alkali metal and halide ions from static and dynamic viewpoints. *J. Phys. Chem. Lett.* **14**, 6270–6277 (2023).

35. Kim, S. L., Lin, H. T. & Yu, C. Thermally chargeable solid-state supercapacitor. *Adv. Energy Mater.* **6**, 1600546 (2016).

36. He, Y. et al. Role of ions in hydrogels with an ionic seebeck coefficient of 52.9 mV K-1. *J. Phys. Chem. Lett.* **13**, 4621–4627 (2022).

37. Cao, J. et al. Stretchable and self-adhesive PEDOT:PSS blend with high sweat tolerance as conformal biopotential dry electrodes. *ACS Appl. Mater. Interfaces* **14**, 39159–39171 (2022).

38. Liu, S. et al. Giant and bidirectionally tunable thermopower in nonaqueous ionogels enabled by selective ion doping. *Sci. Adv.* **8**, eabj3019 (2022).

39. Cheng, H., He, X., Fan, Z. & Ouyang, J. Flexible quasi-solid state ionogels with remarkable seebeck coefficient and high thermoelectric properties. *Adv. Energy Mater.* **9**, 1901085 (2019).

40. He, X., Cheng, H., Yue, S. & Ouyang, J. Quasi-solid state nanoparticle/(ionic liquid) gels with significantly high ionic thermoelectric properties. *J. Mater. Chem. A* **8**, 10813–10821 (2020).

41. Jeong, M. et al. Embedding aligned graphene oxides in polyelectrolytes to facilitate thermo-diffusion of protons for high ionic thermoelectric figure-of-merit. *Adv. Funct. Mater.* **31**, 2011016 (2021).

42. Xue, J. et al. Vapor-activated power generation on conductive polymer. *Adv. Funct. Mater.* **26**, 8784–8792 (2016).

43. Chen, J. et al. A self-sustained moist-electric generator with enhanced energy density and longevity through a bilayer approach. *Mater. Horiz.* **12**, 239–2318 (2025).

44. Wurger, A. Thermoelectric ratchet effect for charge carriers with hopping dynamics. *Phys. Rev. Lett.* **126**, 68001 (2021).

45. Pai, Y. H., Tang, J., Zhao, Y. & Liang, Z. Ionic organic thermoelectrics with impressively high thermopower for sensitive heat harvesting scenarios. *Adv. Energy Mater.* **13**, 2202507 (2023).

46. Jiang, P., Qian, X. & Yang, R. Tutorial: time-domain thermoreflectance (TDTR) for thermal property characterization of bulk and thin film materials. *J. Appl. Phys.* **124**, 161103 (2018).

47. Abraham, M. J. et al. GROMACS: high performance molecular simulations through multi-level parallelism from laptops to supercomputers. *SoftwareX* **1–2**, 19–25 (2015).

48. Martinez, L., Andrade, R., Birgin, E. G. & Martinez, J. M. PACKMOL: a package for building initial configurations for molecular dynamics simulations. *J. Comput. Chem.* **30**, 2157–2164 (2009).

49. Wang, J., Wolf, R. M., Caldwell, J. W., Kollman, P. A. & Case, D. A. Development and testing of a general amber force field. *J. Comput. Chem.* **25**, 1157–1174 (2004).

50. Bussi, G., Donadio, D. & Parrinello, M. Canonical sampling through velocity rescaling. *J. Chem. Phys.* **126**, 14101 (2007).

51. Parrinello, M. & Rahman, A. Polymorphic transitions in single crystals: a new molecular dynamics method. *J. Appl. Phys.* **52**, 7182–7190 (1981).

52. Essmann, U. et al. A smooth particle mesh Ewald method. *J. Chem. Phys.* **103**, 8577–8593 (1995).

53. Humphrey, W., Dalke, A. & Schulten, K. VMD: visual molecular dynamics. *J. Mol. Graph.* **14**, 33–38 (1996).

54. Zhao, C. et al. Moisture-gradient-enhanced ionic thermoelectrics. *Figshare*. <https://doi.org/10.6084/m9.figshare.29613458> (2025).

## Acknowledgements

The authors acknowledge the financial support from the National Key R&D Program of China (2024YFE0217300).

## Author contributions

C.Z. and W.M. conceived the idea and wrote the manuscript. C.Z. was in charge of experimental design and data collection. Y.W. and D.S. conducted the MD simulation and theoretical analysis. X.Z. provided guidance for the experiments. W.M. supervised the project. All authors discussed the results and commented on the manuscript.

## Competing interests

The authors declare no competing interests.

## Additional information

**Supplementary information** The online version contains supplementary material available at <https://doi.org/10.1038/s41467-025-66027-w>.

**Correspondence** and requests for materials should be addressed to Weigang Ma.

**Peer review information** *Nature Communications* thanks Senentxu Lanceros-Mendez and the other anonymous reviewer(s) for their contribution to the peer review of this work. A peer review file is available.

**Reprints and permissions information** is available at <http://www.nature.com/reprints>

**Publisher's note** Springer Nature remains neutral with regard to jurisdictional claims in published maps and institutional affiliations.

**Open Access** This article is licensed under a Creative Commons Attribution-NonCommercial-NoDerivatives 4.0 International License, which permits any non-commercial use, sharing, distribution and reproduction in any medium or format, as long as you give appropriate credit to the original author(s) and the source, provide a link to the Creative Commons licence, and indicate if you modified the licensed material. You do not have permission under this licence to share adapted material derived from this article or parts of it. The images or other third party material in this article are included in the article's Creative Commons licence, unless indicated otherwise in a credit line to the material. If material is not included in the article's Creative Commons licence and your intended use is not permitted by statutory regulation or exceeds the permitted use, you will need to obtain permission directly from the copyright holder. To view a copy of this licence, visit <http://creativecommons.org/licenses/by-nc-nd/4.0/>.

© The Author(s) 2025